Geometric deep learning framework for de novo genome assembly

Lovro Vrcek, Xavier Bresson, Thomas Laurent, et al.

Genome Res. published online October 29, 2024
Access the most recent version at doi:10.1101/gr.279307.124

Geometric deep learning framework for *de novo* genome assembly

Authors:

Lovro Vrček[1,2]*, Xavier Bresson[3], Thomas Laurent[4], Martin Schmitz[1,3], Kenji Kawaguchi[3], Mile Šikić[1,2]*

[1]Genome Institute of Singapore, A*STAR, Singapore

[2]Faculty of Electrical Engineering and Computing, University of Zagreb, Zagreb, Croatia

[3]School of Computing, National University of Singapore, Singapore

[4]Department of Mathematics, Loyola Marymount University, Los Angeles, CA, USA

*Corresponding authors: lovro_vrcek@gis.a-star.edu.sg , mile_sikic@gis.a-star.edu.sg

Running title: *De novo* genome assembly with deep learning

Abstract:

The critical stage of every *de novo* genome assembler is identifying paths in assembly graphs that correspond to the reconstructed genomic sequences. The existing algorithmic methods struggle with this, primarily due to repetitive regions causing complex graph tangles, leading to fragmented assemblies. Here, we introduce GNNome, a framework for path identification based on geometric deep learning that enables training models on assembly graphs without relying on existing assembly strategies. By leveraging only the symmetries inherent to the problem, GNNome reconstructs assemblies from PacBio HiFi reads with contiguity and quality comparable to those of the state-of-the-art tools across several species. With every new genome assembled telomere-to-telomere, the amount of reliable training data at our disposal increases. Combining the straightforward generation of abundant simulated data for diverse genomic structures with the AI approach makes the proposed framework a plausible cornerstone for future work on reconstructing complex genomes with different ploidy and aneuploidy degrees. To facilitate such developments, we make the framework and the best-performing model publicly available, provided as a tool that can directly be used to assemble new haploid genomes.

Introduction

De novo genome assembly provides essential insights into organism's biology and evolution by reconstructing its genome from short DNA fragments (or reads), without the access to the original genomic sequence. The assembly process is based on intricate methods on strings and graphs which were first introduced by Esko Ukkonen (Peltola et al. 1984) and later enhanced by Eugene Myers (Myers 1995) and many other scholars. This approach is known as the Overlap-Layout-Consensus (OLC) paradigm, and the initial step is to build an assembly graph where each node represents an individual read, wheras pairs of overlapping reads are linked by an edge. The next step, layout, is tasked with placing the reads in the correct order—which is equivalent to finding a path through the graph—and is the core of the genome assembly. An alternative paradigm, based on finding paths in de Bruijn graphs, has been developed shortly after (Idury and Waterman 1995; Pevzner et al. 2001) and these two *de novo* assembly approaches are the most common ones today.

The OLC method does have its challenges. Identifying a path in the graph where each node is visited only once is an NP-complete problem. Furthermore, due to imperfections in the overlap algorithms, certain edges are erroneously missing or falsely present. As a result, much of the research has shifted towards graph simplification, where spurious nodes and edges are eliminated (Myers 2005; Li 2016; Zerbino and Birney 2008; Brankovic et al. 2016; Vaser and Šikić 2021). In many regions, these refined methods yield unique solutions. However, they struggle to handle highly complex, repetitive regions in the graph, and resort to cutting them out. The approaches based on de Bruijn graphs are also often unable to find a unique solution in such regions. Thus, the problem of fragmentation in *de novo* genome assembly persists, unless different types of data and manual curation are used, leading to a slower, more expensive assembly. For more information about the computational methods for genome assembly, readers can refer to (Garg 2021) and (Garg et al. 2022).

Recently, a tremendous achievement has been acccomplished through a combination of both different types of data and manual curation—the complete reconstruction of the human genome (Nurk et al. 2022). This was primarily enabled by the latest advancements in the sequencing technologies, with PacBio HiFi reads and ONT ultra-long reads at the forefront. While the HiFi reads are around 15 kilobases (kb) in length and with error rate of less than 0.5%, the ONT ultra-long reads have error-rates around 5%, but can reach the length of over 100 kb (Li and Durbin 2024). Even though using a combination of these complementary reads achieves state-of-the-art assemblies (Cheng et al. 2024), certain regions of the human genome had to be resolved manually in order to ensure correctness.

This, and similar accomplishments enabled us to develop a novel paradigm for *de novo* assembly, one based on geometric deep learning (Bronstein et al. 2021). Here we present GNNome, a framework which uses an accurate, manually-currated reference genome to produce an arbitrary number of training samples, allowing us to train a model based on graph neural networks (GNNs) (Scarselli et al. 2009) and detect paths in the graph corresponding to genome reconstruction. The model presented here, which we make publicly available, yields assemblies with contiguity and quality comparable to the assemblies of the state-of-the-art tools, even though no a-priori knowledge about the algorithmic simplification steps is implemented into the framework. The models trained only on HiFi graphs can produce meaningful assemblies from ONT data as well, although such direct transfer is suboptimal both for the AI methods and the algorithmic approaches. Nonetheles, the framework itself is agnostic to the underlaying sequencing technology and can adapt to both HiFi and ONT assembly graphs.

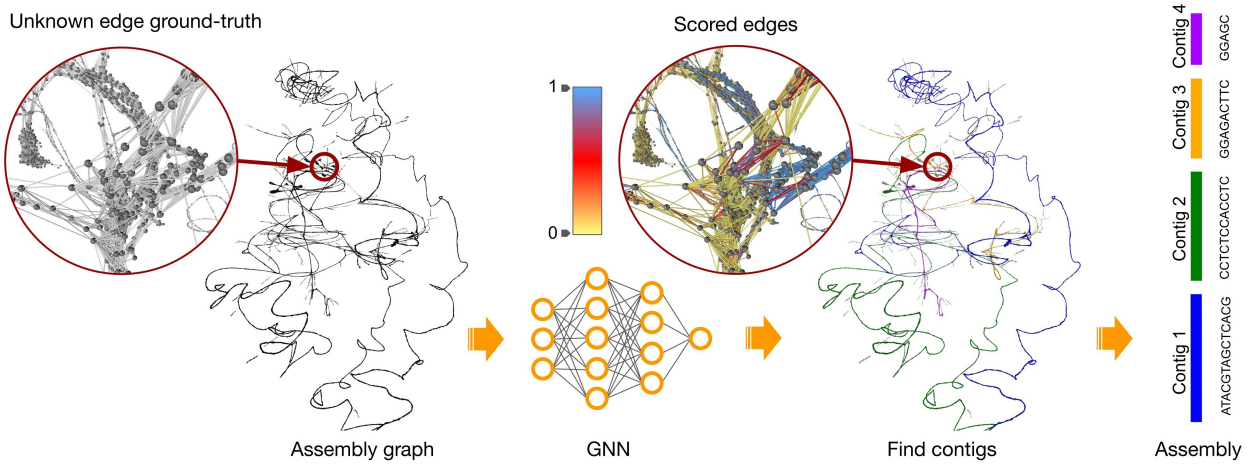

Figure 1. Overview of the assembly workflow with GNNome. An assembly graph is passed to a trained neural network which produces a probability for each edge. The probabilities are visualized in the zoomed-in region in the middle, with the color scheme that increases the visibility of the edges with probability around 0.5. The graph shown here represents entangled Chromosomes 21 and 22 of CHM13 (Nurk et al. 2022) generated with hifiasm (Cheng et al. 2021), as well as the four longest contigs found by GNNome. The graph was visualized with Graphia (Freeman et al. 2022).

Results

Overview of the GNNome framework

General overview of assembling genomes with GNNome is shown in Fig. 1. It starts with an assembly graph, constructed solely using either PacBio HiFi or ONT reads by an OLC-based genome assembler. Such a graph is passed to a trained model (Supplemental Fig. S1) which assigns a probability to each edge in the graph, reflecting the likelihood that the edge contributes to the optimal assembly. Subsequently, a certain number of edges is sampled as starting points for a search algorithm, which navigates through the probabilities with each walk resulting in a contig (Methods). We demonstrate that a well-trained model can confidently guide a search algorithm to avoid incorrect edges.

In conventional assemblers, the assembly graphs are typically simplified with the removal of transitive edges (Myers 2005), trimming of dead-ends (Li 2016), and popping of bubbles (Zerbino and Birney 2008). While these steps are generally reliable and effective, they greatly reduce the number of edges in the graph and thus diminish the amount of information conveyed in the GNN's message passing. Therefore, we use graphs prior to any simplifications.

The model presented in this study was trained on a dataset constructed from six chromosomes of the human HG002 reference genome (Wang et al. 2022b; Rautiainen et al. 2023) using the PBSIM3 simulator (v3.0.0) (Ono et al. 2022), while the validation dataset, constructed in the same fashion, consisted of five different chromosomes (Methods). The assembly graphs were generated with hifiasm (v0.18.7-r514) (Cheng et al. 2021) as it produces state-of-the-art HiFi-only assemblies, although any OLC-based assembler could be used. Using the saved information about the reads, we implement an algorithm alike breadth-first search (BFS) that determines the label for each edge in the constructed training graphs, allowing for a supervised training of the model (Methods).

Most of the existing algorithms for *de novo* assembly are hand-crafted and their parameters are tuned to several well-known genomes. Usually, it is uncertain whether the good performance transfers to other genomes as well, and fine-tuning the algorithm parameters from scratch for a new set of genomes can be tedious. Here, learning based methods facilitate transferability, as the new genomes can easily be introduced into the training set and the model can be retrained with minimal modifications to the framework.

In this work, we borrow the terminology and the definition of assembly graph from miniasm (Li 2016), where the assembly graph is symmetric since each read is represented with two nodes—one representing the original sequence, and its virtual pair representing the reverse-complement of that sequence (Fig. 2A). Such a definition also ensures that the graph is directed instead of bidirected (Edmonds and Johnson 2003) as some representations are (Myers 2005), which would complicate training of the neural network. To utilize these symmetries during training, we devise a novel GNN layer named SymGatedGCN (Methods, Supplemental Fig. S2) and use a loss symmetric with respect to the strand (Fig. 2C). These symmetries were also addressed in several data augmentation steps during the training, such as masking and partitioning of the graph (Fig. 2B) as well as running a search algorithm over the edge probabilities (Fig. 2D). For more details, see Methods.

Since our methodology is optimized for haploid genome assembly, we evaluate GNNome on the homozygous human genome CHM13 (Nurk et al. 2022) derived from a hydatidiform mole, along with the inbred genomes of *M. musculus* (Hon et al. 2020) and *A. thaliana* (Wang et al. 2022a), all of which are backed by high-quality reference genomes. Additionally, we evaluate on a maternal genome of *G. gallus* (Vertebrate Genome Project), for which the sequencing data was obtained with trio binning.

Contiguity is one of the critical aspects of genome assembly and it is typically assessed using NG50 and NGA50 metrics. GNNome is run on the assembly graphs generated by hifiasm (Cheng et al. 2021) from

HiFi reads and achieves similar or higher NG50 and NGA50 than the respective assembler while relying only on the predicted edge-probabilities. The overview of these results can be seen in Fig. 3. A more detailed analysis, including other measures and the comparison with the state-of-the-art tools as well as transferability to ONT data, is presented in Tables 1 and 2.

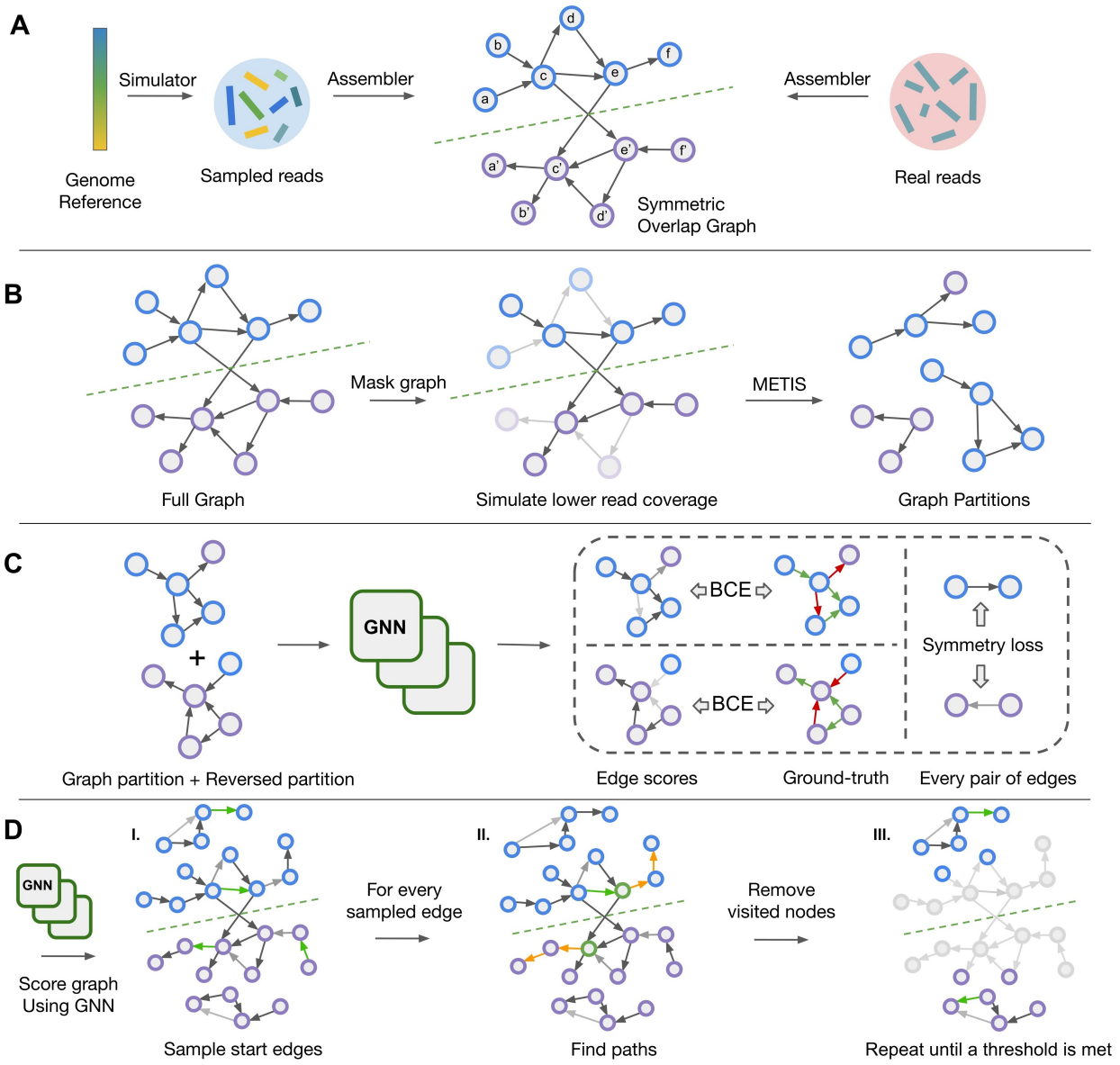

Figure 2. Schematic visualization of the training and decoding pipeline. (*A*) Generating and processing of the synthetic reads for training and real reads for inference**.** Different colors of the simulated reads indicate that their positions on the reference genome are known, unlike the positions of the real reads. The green dashed line shows the line of mirror symmetry. (*B*) Data augmentation during training. The grayed-out nodes and edges are the ones that are masked. (*C*) Training the model by computing the strand-wise symmetric loss over the edges. The shade of the edges indicates the values of the scores, while red and

142 green color indicates negative/positive edge labels. (*D*) Iterative decoding on a new graph during inference.
143 Green nodes indicate the starting edges for walks, and orange edges represent the steps taken by a
144 decoding algorithm. The grayed-out nodes and edges represent the ones that are previously traversed and
145 are thus discarded in the next iteration of the decoding algorithm.

146

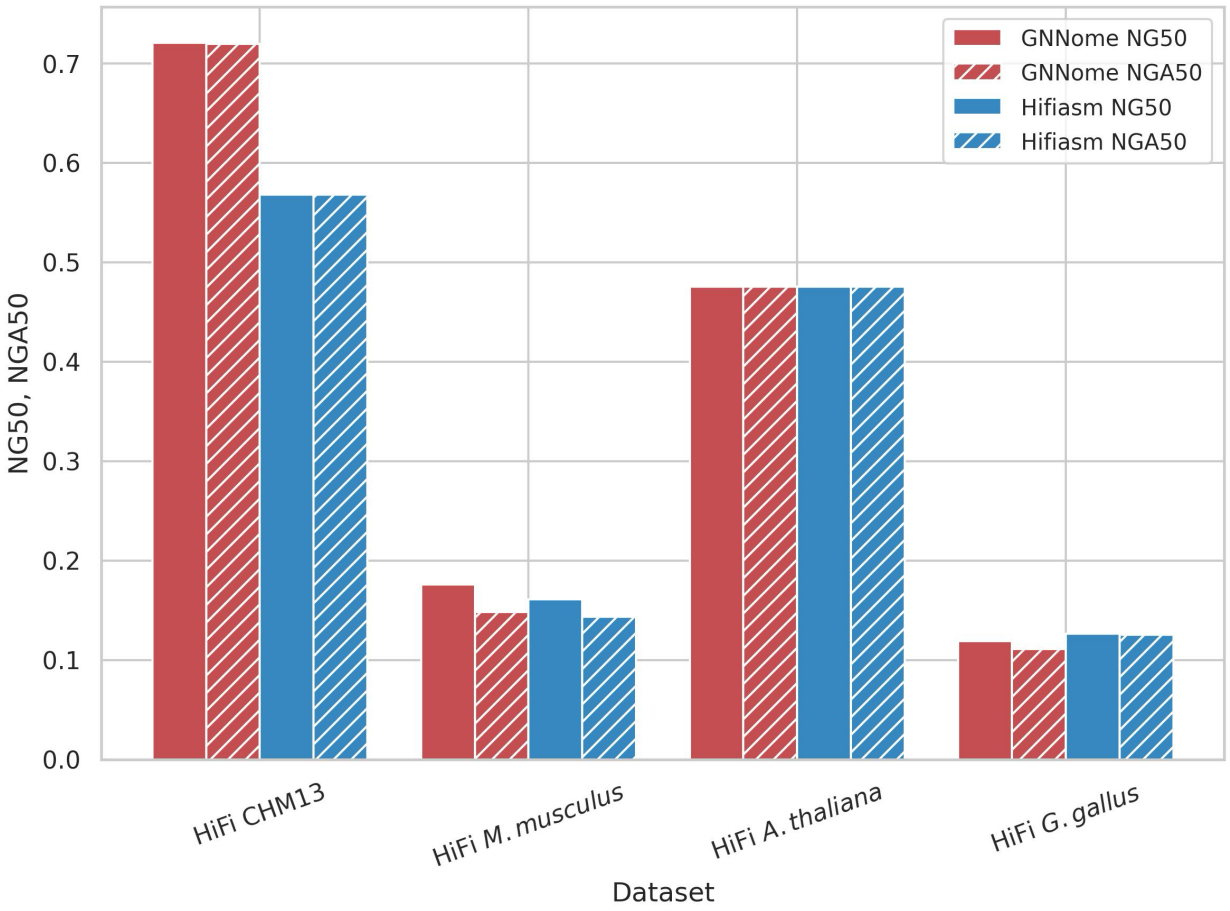

147

148

149 **Figure 3.** Contiguity on different haploid datasets. Comparison of contiguity of assemblies generated with
150 GNNome and hifiasm (Cheng et al. 2021) for HiFi data. The NG50 of the assembly is defined as the
151 sequence length of the shortest contig that, together with longer contigs covers the 50% of the total
152 genome. The NGA50 is computed similarly like NG50, but instead of considering contigs, we consider
153 blocks correctly aligned to the reference. Both NG50 and NGA50 are presented as proportions of the
154 maximum achievable NG50 (NGA50) values for each respective genome.

155

Assembling HiFi datasets

We first evaluate GNNome (v0.4.0) along with hifiasm (v0.18.7-r514) (Cheng et al. 2021), which was used to construct the starting assembly graphs provided to GNNome, on four HiFi samples—CHM13 (Nurk et al. 2022), C57BL/6J strain of *M. musculus* (Hon et al. 2020), Col-0 strain of *A. thaliana* (Wang et al. 2022a), and *G. gallus* maternal genome (bGalGal1 isolate obtained from Vertebrate Genome Project). The coverages of these samples are roughly 32×, 25×, 35×, and 30×, respectively. Additionally, on the same datasets we evaluate HiCanu (v2.2) (Nurk et al. 2020) and Verkko (v1.4.1) (Rautiainen et al. 2023), both popular *de novo* assemblers. Although hifiasm and Verkko can utilize different types of data in their pipelines, here we focus on HiFi-only assembly.

From Table 1 we see that GNNome achieves higher NG50 and NGA50 on CHM13 and *M. musculus* than hifiasm by 25% and 3%, respectively. In the case of *A. thaliana*, the NGA50 is the same for both methods, and on *G. gallus* GNNome lags behind hifiasm by 11%. When evaluating on *G. gallus*, HiCanu encountered an error after running for 14 days. On the other three datasets, HiCanu achieved lower contiguity by 30% or more. Similarly, Verkko also achieves lower contiguity across the datasets, by more than 15%. It is also worth noting that in case of *A. thaliana*, the length of the GNNome's assembly is the closest to the length of the reference. We hypothesize that the difference in the contiguity improvements GNNome achieves on CHM13 compared to other genomes stems from more similar graphs seen during the training phase. If this hypothesis proves correct, adding new, high-quality, telomere-to-telomere genomes to the training set as they appear will lead to higher quality reconstructions of non-human genomes. We discuss training data in Methods.

In addition to contiguity of the assemblies, we evaluated their gene completeness, quality values (QVs), and misassemblies. While the percentage of duplicated genes on CHM13 and *A. thaliana* is similar for GNNome, hifiasm and Verkko, for HiCanu it is considerably higher. The percentage of complete genes is

the lowest for Verkko, while for the other three approaches it is similar. On *M. musculus* and *G. gallus*, however, it is GNNome that has more duplicated genes than the other three assemblers. The graph of *M. musculus* seems to be substantially more complex than that of CHM13, even though the *M. musculus* genome is slightly shorter and the coverage of the corresponding read sample is also lower. While the CHM13 graph has 2.4 million nodes and 18.5 million edges, the *M. musculus* graph has 3.7 million nodes and 44.6 million edges. We assume that this higher graph complexity led to lower contiguity and higher percentage of duplicated single-copy genes.

In terms of quality, GNNome produces assemblies with slightly lower QV for CHM13 and *G. gallus* than hifiasm, but with a notably higher QV than assemblies of all the other tools on *A. thaliana*. Similarly, the number of GNNome's structural misassemblies is higher on CHM13 and *G. gallus*, and comparable or lower than that of other assemblers on *M. musculus* and *A. thaliana*. We analyze the misassemblies of GNNome and hifiasm on CHM13 and find that 21 out of 44 of GNNome's structural misassemblies come from Chromosomes 9 and 16 (Supplemental Fig. S3). Moreover, we observe that GNNome and hifiasm produce misassemblies on different chromosomes rather than always on the same ones. For example, on Chromosome 2 GNNome has 44 local misassemblies and hifiasm has only 1, while on Chromosome 18 hifiasm has 71 local misassembly and GNNome has none (Supplemental Fig. S3). This analysis indicates that GNNome provides an alternative way to assemble genomes as compared to hifiasm, even though the underlaying assembly graphs are the same.

Another notable difference between the CHM13 assemblies of GNNome and hifiasm is in the case of Chromosome 11 (Fig. 4A-B). Whereas hifiasm splits a tangle in the centromeric region into three different contigs (Fig. 4B), GNNome manages to correctly traverse the nodes in the tangle, leading to no breaks and no repetitiveness (Fig. 4A).

Next, we analyze how different assemblers resolve regions with perfect repeats by setting up a simulation with a short, synthetic genome carrying a variable number of identical repeat units. The number of repeat units varies from 2 to 15, covering cases both where reads easily bridge the entire repetitive region and when they do not. We observe that not only do all the tested assemblers commonly produce misassemblies, but also that GNNome and hifiasm produce highly similar assemblies in nearly all scenarios (Supplemental Note S1, Supplemental Fig. S4). One exception, when their assemblies are different, is visualized in Supplemental Fig. S5. This high similarity between GNNome's and hifiasm's assemblies implies that the degree to which a repeat can be resolved heavily depends on the overlap phase of the assemblers, which is shared between GNNome and hifiasm.

It is noteworthy that the model underwent training on graphs of notably smaller sizes—graphs of individual chromosomes further partitioned with METIS (Karypis and Kumar 1998) contained roughly 50 thousand nodes (Methods). Meanwhile, the full graph of the CHM13 genome graphs consists of 2.3 million nodes, showing that the model can generalize well to graphs even 50 times larger and substantially more complex.

Table 1. Results on HiFi reads. The best achieved results are in **bold**. Size is the total length of the assembly. The lengths of the references are 3,054 Mb, 2,728 Mb, 133 Mb, and 1,053 Mb for CHM13 (v1.1), *M. musculus* (GRCm39), *A. thaliana* (Col-XJTU), and *G. gallus* (bGalGal1 maternal) respectively. The LG50 (LG90) measure is the smallest number of contigs that together cover 50% (90%) of the genome. NG50 and NGA50 were computed with minigraph (Li et al. 2020). "Complete" gives the percentage of the reference single-copy genes that are found in the assembly genome, while "duplicated" gives the percentage of reference single-copy genes that are aligned to multiple positions in the assembly. Both "complete" and "duplicated" were computed with compleasm (Huang and Li 2023). QV is per-base consensus accuracy, computed with yak by comparing *k*-mers in contigs to *k*-mers found in short reads (Cheng et al. 2021). Short reads were not available for *G. gallus*, so we computed QV with PacBio HiFi reads instead. Number of structural and local misassemblies (# misasm) was computed with QUAST (Mikheenko et al. 2018). Full QUAST report for HiFi data is given in Supplemental Table S1.

Dataset	Assembler	Size [Mb]	LG50	LG90	NG50 [Mb]	NGA50 [Mb]	Complete [%]	Duplicated [%]	QV	# misasm structural	# misasm local
CHM13	**GNNome**	3,051	**12**	**31**	**111.3**	**111.0**	99.53	0.71	54.24	44	86
	Hifiasm	**3,052**	**12**	32	87.7	87.7	**99.55**	**0.70**	**55.86**	**23**	101
	HiCanu	3,297	16	57	69.7	69.7	99.54	2.79	43.30	24	51
	Verkko	3,030	101	348	9.4	9.4	99.44	0.77	51.61	43	**30**
M. musculus	**GNNome**	2,643	**38**	**140**	**23.0**	**19.3**	**99.62**	3.30	45.40	707	1053
	Hifiasm	2,613	40	150	21.1	18.7	**99.62**	**1.93**	45.67	706	1007
	HiCanu	**2,651**	67	271	11.2	10.5	99.56	2.65	43.77	781	1205
	Verkko	2,609	54	204	15.9	14.6	99.60	1.95	**45.72**	**705**	**1005**
A. thaliana	**GNNome**	**139**	**5**	**13**	**12.4**	**12.4**	99.89	1.09	**52.08**	129	90
	Hifiasm	151	**5**	**13**	**12.4**	**12.4**	**99.90**	1.07	44.52	342	56
	HiCanu	152	6	16	8.6	8.6	99.87	3.20	40.30	**106**	**52**
	Verkko	158	6	18	10.3	10.3	99.87	**1.04**	39.75	229	54
G. gallus	**GNNome**	1,114	31	135	10.8	10.1	95.79	2.99	49.35	2434	8391
	Hifiasm	**1,087**	**27**	**123**	**11.5**	**11.4**	**96.14**	2.03	**51.08**	2164	7231
	Verkko	1,041	83	410	3.8	3.7	95.44	**1.08**	49.65	**1340**	**3819**

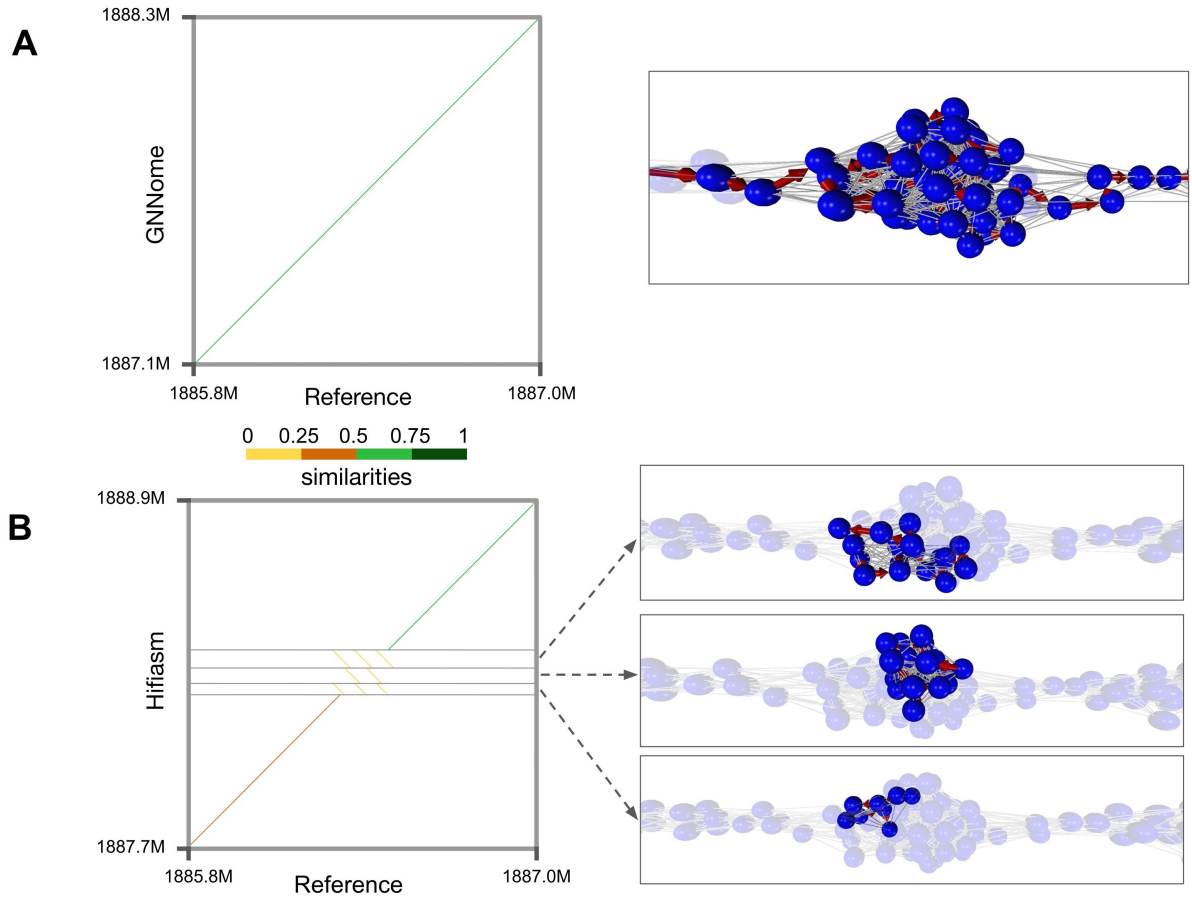

Figure 4. Assembly comparison of Chromosome 11 centromeric region. (*A*) GNNome's assembly of the region. (*B*) Hifiasm's assembly of the region. Mappings of the assembly to the reference are visualized with dotplots, which were created with D-Genies (Cabanettes and Klopp 2018)—a tool based on minimap2 (Li 2018) alignment. The nodes that comprise each contig are visualized on the right with the help of Graphia (Freeman et al. 2022). The region covered by the tangle is around 264.5 kb long.

Assembling ONT datasets

We investigate whether the model trained only on HiFi graphs can also generalize to ONT graphs constructed with Raven (v1.8.1) (Vaser and Šikić 2021), without ever seeing any ONT data. Although the idea seems far-fetched at first, both assemblers follow the same sequence alignment principles and construct the graphs in the same fashion, only from the different underlying data. For this purpose, we compare the GNNome's assemblies of CHM13 and Col-0 strain of *A. thaliana* with Raven's, starting from the same assembly graphs. The coverage of both samples is roughly 120×. Additionally, we also compare with two other popular assembler for ONT reads, Flye (v2.9.2-b1786) (Kolmogorov et al. 2019) and Shasta (v0.11.1) (Shafin et al. 2020). The results are available in Table 2.

On CHM13, GNNome again achieved far higher NG50 and NGA50 than any other assembler. However, we notice a gap between NG50 and NGA50, which is also accompanied by a higher number of misassemblies and lower QV. On *A. thaliana* NG50 and NGA50 are of similar values, and comparable to those achieved by Raven. The number of complete single-copy genes on *A. thaliana* is higher than for other tools, but so is the number of misassemblies. We observe that Raven also has a notably higher number of misassemblies than Flye and Shasta, and hypothesize that the large amount of GNNome's misassemblies can partially be attributed to relying on Raven's overlap phase. It is also worth noting that Flye and Shasta are not based on the OLC paradigm, but rather on de Bruijn graph approach. Both of these assemblers achieve an order of magnitude less misassemblies on both datasets, though also lower contiguity—except for Flye's assembly of CHM13, whose contiguity is comparable to Raven's.

The results suggest that, while the general idea of the framework can be transferred to ONT reads and the assemblies produced by GNNome are still meaningful, directly transferring the model to a different type of data is not the optimal solution. This also indicates topological differences between HiFi and ONT graphs. Better results might be achieved by training the model on ONT data from scratch, but this approach

is not practical from the computational standpoint. The ONT datasets typically have a sequencing depth above 100-fold, considerably higher than the HiFi ones, while also containing sequences of longer lengths. This makes the creating of the read samples, as well as generating the graphs, notably slower. Despite this, the resulting graphs are around two orders of magnitude smaller than the HiFi graphs, primarily due to many reads being discarded as contained. For example, the hifiasm-constructed graph of human Chromosome 1 from reads with 60-fold coverage has 311 thousand nodes and 4.1 million edges, while Raven-constructed graph from ONT reads with 120-fold coverage has only 5.6 thousand nodes and 22 thousand edges. Thus, to have the same number of edges in the training set, for each HiFi graph we would require substantially more ONT graphs—making the dataset preparation considerably more computationally expensive.

Table 2. Results on ONT data. The best achieved results are in **bold**. The assemblies of GNNome and Raven were additionally polished with Racon (Vaser et al. 2017). Flye and Shasta have built-in polishing modules, so we did not perform additional post-assembly polishing. Shasta did not assemble 90% of the A. thaliana genome, hence the LG90 is undefined. Full QUAST report for ONT data is given in Supplemental Table S2.

Dataset	Assembler	Size [Mb]	LG50	LG90	NG50 [Mb]	NGA50 [Mb]	Complete [%]	Duplicated [%]	QV	# misasm structural	# misasm local
CHM13	**GNNome**	**2,984**	**11**	**27**	**111.0**	**83.1**	99.42	0.83	33.59	1758	1695
	Raven	2,907	16	48	72.6	70.3	**99.51**	0.70	34.04	1146	952
	Flye	2,851	17	60	70.0	69.5	99.50	**0.69**	33.91	134	**123**
	Shasta	2,884	17	72	59.7	56.3	99.50	0.55	**37.30**	**57**	190
A. thaliana	**GNNome**	**131**	**4**	**9**	**14.6**	**14.5**	**99.83**	1.07	26.54	242	221
	Raven	125	5	11	14.5	**14.5**	99.81	1.07	**27.28**	95	185
	Flye	124	5	15	13.7	13.7	99.79	1.07	26.03	**7**	**16**
	Shasta	115	5	-	12.1	12.1	99.81	**0.94**	25.84	16	256

Comparing different layout algorithms

It might be assumed that layout algorithms are interchangeable among different genome assemblers, offering little benefit from new implementations. However, when we applied Raven's layout process to hifiasm-generated graphs, the results contradicted this assumption. According to Supplemental Table S3, the performance of Raven's algorithm significantly lagged behind hifiasm's when applied to the same assembly graphs. Specifically, the NG50 and NGA50 metrics for Raven were roughly 25-50% lower than those achieved by hifiasm across all four evaluated genomes, demonstrating the distinct effectiveness of layout algorithms.

This indicates that tailoring assembly algorithms to the particular type of assembly graphs may be present in the existing *de novo* assemblers. Worse performance of Raven's layout on hifiasm's graphs is similar to what we observed when we transferred the GNNome model trained only on hifiasm graphs to ONT data. This experiment further shows that direct transfer of methods to a different type of data is not the optimal strategy, both for the algorithms and machine learning models.

SymGatedGCN outperforms other GNN layers

SymGatedGCN layer was inspired by GatedGCN (Bresson and Laurent 2017) due to its performance on several benchmarks (Dwivedi et al. 2020), but additionally includes an edge feature representation and uses a dense attention map for the edge gates (Bresson and Laurent 2019; Joshi et al. 2019). Furthermore, most off-the-shelf GNN layers are devised for undirected graphs. In our earlier efforts (Vrček et al. 2022), we noticed that this is a significant limitation when working with directed graphs. Thus, we devise a bidirectional message-passing procedure with an independent set of trainable parameters for each

direction (Methods, Supplemental Fig. S2). Our findings on training on directed graphs were later more formally confirmed (Rossi et al. 2023).

First, we test the effectiveness of SymGatedGCN against a baseline—a model that predicts the same score for every edge, resulting in random walks during the decoding. We demonstrate that random walks vastly underperform when compared to decoding with the model scores (Supplemental Note S2, Supplemental Fig. S6).

Next, we compare the performance of SymGatedGCN to other popular GNN layers—GCN (Kipf and Welling 2016), GraphSAGE (Hamilton et al. 2017), GAT (Veličković et al. 2017), and GatedGCN (Bresson and Laurent 2017)—which were run on both directed and undirected graphs, and show consistently superior performance of SymGatedGCN (Supplemental Note S2, Supplemental Fig. S7). Additionally, we compare the influence of node and edge features and show that all the features contribute to the performance (Supplemental Note S3, Supplemental Fig. S8).

Discussion

This is the first attempt to solve *de novo* genome assembly using deep learning. Untangling the graph is the central part of the problem, and graph neural networks are perfect for this task—with large amounts of data and complex patterns difficult to recognize, machine learning offers an advantage over engineered algorithms.

Lately, we have seen the increase in the genomes assembled telomere-to-telomere. Those have mostly been achieved with a combination of different types of data and often manual curation, increasing the time and the cost of the assembly. Improving single-technology assembly leads to not only lower time and

cost, but also democratization of assembling new genomes, allowing the laboratories that do not have access to different data types to assemble high-quality draft references.

It is worth noting that all assemblers yield superior results for the human genome compared to other genomes evaluated in this study, likely because of our more comprehensive understanding of human genomics and the greater abundance of such data. This highlights the critical need for intensified efforts toward high-quality genome assemblies of non-human eukaryotic organisms. Similarly, the GNNome model that was trained on a subset of HG002 data achieves the best results on CHM13—both human genomes. As the volume of reliable genome data continues to grow, we anticipate further enhancements in the performance of our deep learning approach, especially on non-human data, and foresee our method serving as a foundation for future approaches designed to leverage this expanding genome dataset.

Drawing inspiration from the pioneering telomere-to-telomere human genome assembly project, which started with a haploid genome (CHM13), our innovative approach also concentrates on haploid assembly. This strategy significantly streamlines the process relative to the assembly of higher ploidy genomes. Moreover, while there exist tools—based on classical algorithms—capable of assembling diploid and even polyploid genomes, they necessitate the use of various sequencing technologies and sequencing of parental genomes to phase the genome reliably. We believe the proposed method can greatly benefit sequence reconstruction when a homozygous or inbred sample is at hand, thereby reducing the need for a large amount of genomic material and cutting sequencing costs, which are often prohibitive. Moreover, the proposed deep learning paradigm, with its capacity to generate abundant simulated datasets and graphs combined with usage of AI methodologies rather than relying on manual inspection and hand-crafted heuristics, is expected to significantly accelerate the development of assembly tools. This advancement will be particularly beneficial for the reconstruction of both diploid and polyploid genomes, as well as in addressing the complexities of aneuploid genomes, where chromosome numbers vary. Such

342 variations are frequently observed in cancerous cells, making this approach highly relevant in cancer
343 research. These more difficult tasks will be the focus of our future work.

344 We demonstrate the applicability of proposed framework to OLC graphs. However, the same approach can
345 be applied to de Bruijn graphs as well. Moreover, many problems in computational genomics including
346 mapping reads to pangenome graphs belong to combinational optimization problems on graphs which are
347 usually computationally intractable, and the proposed framework can be easily adapted to them.

348 Finally, even the best layout algorithms are limited by the graphs they are given. The missing edges that
349 were not created during the graph construction cannot be introduced in layout, at least not with the
350 currently available approaches. The increasing popularity of geometric deep learning could open a new
351 frontier here as well—a deep learning-based method for the overlap phase.

352

Methods

Datasets

For training, the data was simulated from HG002 draft reference (v0.7) (downloaded from HG002 github) and PBSIM3 (Ono et al. 2022). Training set consisted of Chromosomes 1, 3, 5, 9, 12, and 18, while the validation set consisted of Chromosomes 6, 11, 17, 19, and 20. The acrocentric chromosomes were not considered for either set due to their incompleteness in the draft reference. Moreover, we do not use all the chromosomes from the reference in order to better show the generalization capability of our model to full human genome CHM13 – even though not all the chromosomes were seen in either training or validation, our model consistently performs well. The chromosomes chosen for training were sampled 15 times each to produce samples of reads, which resulted in 15 hifiasm-constructed assembly graphs for each chromosome. Similarly, each chromosome in the validation set was sampled 5 times. We present the results of the best performing model's predictions of edge class for each training and validation chromosome in Supplemental Table S4. Each time the sampling of the reference was different, which led to differences in the assembly graphs used for training and validation. This was a convenient way to synthetically increase the size of our dataset. Note that the graph of each chromosome is considered as a separate data point—the network was not trained on a graph of a combination of reads coming from different chromosomes. We show that, while the specific choice of training and validation chromosomes doesn't play a major role in the performance, the number of copies of the chromosomes in the training and validation sets does, as less edges to train on leads to worse performance (Supplemental Note S4, Supplemental Fig. S9, Supplemental Table S5). Additionally, adding data from the recently assembled ape X and Y Chromosomes (Makova et al. 2024) improves the performance, even with less training examples (Supplemental Note S4, Supplemental Fig. S9, Supplemental Table S5). For parsing FASTA/Q files, we used Biopython (Cock et al. 2009).

Labels

The algorithm that determines the label for each edge in the training graphs consists of two steps. In the first step, it utilizes the positional information of each read—start, end, and strand with respect to the reference. It first identifies all edges which are not sampled from the same strand, and which do not have a valid suffix-prefix overlap. More formally, for edge $A \rightarrow B$ connecting nodes A and B, the following relations must hold:

$$A_{strand} = B_{strand}$$

$$A_{start} < B_{start}$$

$$A_{end} > B_{start}$$

$$A_{end} < B_{end}$$

All edges that do not satisfy these criteria are labeled as incorrect and removed from the graph. However, even in such a reduced graph where all the overlaps are valid, not every edge leads to the optimal assembly, the best example being dead ends. Thus, in the second step of the algorithm, a node with the lowest starting position is first identified and BFS is run from it. Of all the visited nodes, the one with the highest end position is picked. Then, we again run BFS, but this time backwards—opposite of the direction of the edges. The edges that are visited by both BFS runs lead to the optimal assembly of that part of the graph and are labeled as positive, while those visited by just one BFS are labeled as negative. In some cases, the assembly graphs can consist of more than one component, so this algorithm is repeated for each of them, until all the edges are labeled. In the implementation of this algorithm, we utilized NetworkX (Hagberg et al. 2008).

The labels we get are highly imbalanced, with around 99.75% of the edges being labeled as positive. This is expected as hifiasm connects nodes with an edge only if the overlap between the corresponding sequences is of high quality. Thus, most of the false overlaps stem from repetitive regions.

SymGatedGCN

Let i and $s \to t$ be the node and the directed edge whose representations we want to update, respectively. We will use st to denote $s \to t$ for simplicity. The node features $x_i \in \mathbb{R}^{d_n}$ and edge features $z_{st} \in \mathbb{R}^{d_e}$ are first transformed into their embeddings in the latent space with linear layers. It was shown that, for low-dimensional features, it is beneficial to encode them into a highly dimensional representations in a two-step process (Laurent et al. 2022). In our case, the node features are only in-degree and out-degree of each node, while the edge features are length and the similarity of the overlap, thus $d_n = d_e = 2$. Similarity is computed as

$$\text{overlap similarity} = \frac{\text{overlap length} - \text{edit distance}}{\text{overlap length}}.$$

Edit distance computes an approximate string matching between a suffix and the prefix of the overlapping reads (Navarro 2001), and was obtained with Edlib (Šošić and Šikić 2017). The embedding of the features is then performed with:

$$h_i^0 = W_2^n(W_1^n x_i + b_1^n) + b_2^n \in \mathbb{R}^d$$

$$e_{st}^0 = W_2^e(W_1^e z_{st} + b_1^e) + b_2^e \in \mathbb{R}^d$$

where h_i^0 is the initial representation of the node i, e_{st} is the initial representation of the edge st, and all the W and b are learnable parameters. The main part of the model consists of a stack of SymGatedGCN layers which update the representations of both the nodes and the edges iteratively. Let the

representations of node i and edge st at layer l be h_i^l and e_{st}^l. Also, let all the predecessors of node i be denoted with j and all its successors with k. Then, the node and edge representations at layer $l+1$ will be computed as:

$$h_i^{l+1} = h_i^l + ReLU\left(BN\left(A_1^l h_i^l + \sum_{j\to i} \eta_{ji}^{f,l+1} \odot A_2^l h_j^l + \sum_{i\to k} \eta_{ik}^{b,l+1} \odot A_3^l h_k^l\right)\right) \in \mathbb{R}^d$$

$$e_{st}^{l+1} = e_{st}^l + ReLU\left(BN\left(B_1^l e_{st}^l + B_2^l h_s^l + B_3^l h_t^l\right)\right) \in \mathbb{R}^d$$

where all $A, B \in \mathbb{R}^{d\times d}$ are learnable parameters, $ReLU$ stands for rectified linear unit, BN for batch normalization, and $\odot$ for Hadamard product. The edge gates are defined as:

$$\eta_{ji}^{f,l} = \frac{\sigma\left(e_{ji}^l\right)}{\sum_{j'\to i} \sigma\left(e_{j'i}^l\right) + \epsilon} \in [0,1]^d$$

$$\eta_{ik}^{b,l} = \frac{\sigma\left(e_{ik}^l\right)}{\sum_{i\to k'} \sigma\left(e_{ik'}^l\right) + \epsilon} \in [0,1]^d$$

where σ is the sigmoid function, and ϵ is a small value to avoid division by zero.

Note that we distinguish between the messages $\eta_{ji}^{f,l}$ passed along the edges, and in the reverse direction of the edges $\eta_{ik}^{b,l}$. The diagram of this layer, inspired by the diagram of GatedGCN (Dwivedi et al. 2020), can be seen in Supplemental Fig. S2.

Finally, we use a multi-layer perceptron (MLP) on the node and edge representations produced by L SymGatedGCN layers to classify the edges. For each directed edge $s \to t$, a probability p_{st} is computed and trained such that it leads to the optimal assembly. The probability is given by passing the concatenated node representation of nodes s and t, as well as the edge representation of the directed edge $s \to t$:

$$p_{st} = \sigma\left(\mathrm{MLP}(h_s^L \| h_t^L \| e_{st}^L)\right) \in [0,1]$$

where σ is the sigmoid function, L denotes the last SymGatedGCN layer and || is the concatenation operator. The diagram of the whole model can be seen in the Supplemental Fig. S1.

Data augmentation during training

All the samples of reads were initially generated with a 60-fold coverage, slightly higher than the typical sequencing depth of HiFi reads (30 to 50-fold). This allows us to utilize the reads more efficiently and virtually increase the size of the dataset through masking (Fig. 2B). Every epoch, a subset of nodes of each 60-fold graph is masked to resemble the coverage of between 25× and 60×, with the exact number being randomly chosen. The nodes to be masked are also chosen randomly, so each graph can be reused many times as an entirely new data point. Additionally, masking of the nodes is done in a strand-wise manner to retain the symmetry of the assembly graph—either both the node and its virtual pair are masked, or neither of them is.

Since the graphs are simulated from different chromosomes, and then even further reduced while simulating different coverages, their sizes vary greatly. Moreover, training even on the smallest graphs would exceed the graphical processing unit's (GPU's) memory. Thus, we partition them into smaller partitions of uniform sizes with METIS (Karypis and Kumar 1998) (Fig. 2B). This ensures that the partitions are roughly uniform in size and that they can be loaded into a GPU memory, which would otherwise be impossible given that even the smallest graphs in the training set consist of approximately 80,000 nodes and 800,000 edges. METIS partitions the graph by cutting the least number of edges needed to achieve a certain number of partitions. Since the edges connecting these partitions are cut out, the model would not make predictions on them during the training, which might hinder the predictions on the similar edges in the inference. Therefore, we add 1-hop neighborhood to each partition to tackle this issue (He et al. 2022).

Learning objective

The learning objective of the task is binary edge classification, where for each edge the model is predicting whether it leads to the optimal assembly if traversed during the decoding. We utilize the symmetry of the graph and the fact that if an edge $A \rightarrow B$ leads to the optimal solution, then necessarily the edge $B' \rightarrow A'$, connecting the virtual pairs of nodes A and B, also leads to the optimal solution on the reverse strand (Fig. 2C). More concretely, we devise a loss symmetric with respect to the strand:

$$\mathrm{Loss}(e, e') = \mathrm{BCE}(p_e, y_e) + \mathrm{BCE}(p_{e'}, y_{e'}) + \alpha |l_e - l_{e'}|,$$

where BCE stands for binary cross entropy, $\alpha \geq 0$ is a scalar, e and e' are an edge and its virtual pair, whereas p, y, and l denote probability, label, and logit corresponding to the edge e or e'.

To compute such loss of a certain set of edges, each partition should also include their virtual pairs. This is not guaranteed by METIS. Thus, for each partition a virtual partition is also created, with all the edges reversed, to facilitate the computation of the strand-wise symmetric loss. Those two partitions are considered as a mini-batch, and the backpropagation was performed on the loss averaged over all the edges in the partition (Fig. 2C).

Training setup

The model used in this study had latent dimension $d = 64$, number of GNN layers $L = 8$, and 3 layers in the MLP classifier. Node and edge features were first linearly transformed to 16-dimensional tensors and then to the 64-dimensional latent space. This results in roughly 220,000 parameters—a small model compared to today's standards. Dropout of 0.2 was used on node representations after every GNN layer. METIS partitions consisted of roughly 50,000 nodes. The scaling factor α in the loss was 0.1. The network

was trained with Adam (Kingma and Ba 2014) optimizer with initial learning rate of 10^{-4} and decay of 0.95 after 2 consecutive epochs of no improvement in the loss on the validation set. Test set, consisting of real genomes presented in Table 1, was held out during the training. Minimal validation loss values of the trained models can be found in Supplemental Table S6. The results In Tables 1 and 2 correspond to the model with the lowest validation loss.

The training was done on a single Nvidia A100 GPU with 40 gigabytes (GB) of memory and took around 9 hours and 15 minutes. For training the network, we used Python (Van Rossum and Drake 2009), PyTorch (Paszke et al. 2019), DGL (Wang et al. 2019), and NumPy (Harris et al. 2020). DGL utilized 32 threads on AMD EPYC 7702 64-Core processor.

Decoding and inference setup

At inference, METIS is not used in order to avoid cutting any edges in the graph. Thus, we cannot load full graphs into a GPU memory, and instead run inference on a central processing unit (CPU). We perform this on AMD EPYC 7742 processor. A full graph is passed to a trained model, which produces a probability for each edge. The next step is to decode these probabilities and obtain paths representing the genome reconstruction. This is done by sampling the starting edges and running a greedy search from them. Once again, due to the nature of the graph, we opt for the symmetric approach—after sampling a certain number of starting edges, the greedy search in the forward direction is run from the target node of each chosen starting edge, whereas the backward search is run from the virtual pair of the starting edges' source node (Fig. 2D). The nodes that are not traversed, yet they have a predecessor and a successor that are traversed consecutively, are labeled as visited and discarded—this is equivalent to traversing a transitive edge.

We investigate how the number of starting edges in the decoding influences contiguity. As expected, the higher the number of starting edges, the better the contiguity of the genome, as there is a higher chance that a valid path will be found. However, after increasing the number of starting edges from 100 to 250, on most of the datasets the average results improve only slightly or not at all (Supplemental Note S5, Supplemental Fig. S10). Thus, 100 starting edges gives a good tradeoff between the contiguity and the execution speed. The decoding is performed until the found contigs are longer than 70kb. We noticed that if we keep decoding for shorter contigs, this significantly increases execution time and the number of duplications in our assemblies, stemming from the fact that we use non-reduced assembly graphs.

Time and memory consumption

We report the time and memory needed for executing the assembly pipeline, both for our method and for other assemblers. The comparison with the other assemblers is not entirely fair, due to the fact that we cannot independently evaluate different parts of their assembly pipelines, such as read overlap, graph construction, and layout. Thus, the time and memory consumption of the other assemblers is provided for their entire pipeline, whereas for our tool we measure each stage independently. Nevertheless, we believe that such analysis gives an insight into the complexity of our approach and the approach of the assemblers, showing that our method is not a bottleneck in the pipeline. These results can be found in Supplemental Table S7.

Data sets analyzed

All data used in this study is publicly available. For training, we used HG002 draft reference v0.7 which can be found at https://github.com/marbl/HG002. HiFi CHM13 dataset, sequenced with the depth of ~32×, is available under accessions SRR11292120, SRR11292121, SRR11292122, and SRR11292123. *M. musculus* dataset, sequenced with ~25× coverage, is available under accession SRR11606870. *A. thaliana* dataset, sequenced with ~157× coverage and downsampled to ~35× with SeqKit (Shen et al. 2016) v2.5.1, is available at https://ngdc.cncb.ac.cn/gsa/browse/CRA004538/CRX257575. *G. gallus* HiFi dataset, sequenced with ~77× coverage was downsampled to ~30× with SeqKit and is available https://www.genomeark.org/genomeark-all/Gallus_gallus.html. Parental Illumina short reads of *G. gallus*, used in trio-binning, are available at the same link.

ONT CHM13 dataset is available at https://github.com/marbl/CHM13. *A. thaliana* ONT dataset, sequenced with 388× and downsampled to ~120× with SeqKit, is available at https://ngdc.cncb.ac.cn/gsa/browse/CRA004538/CRX257574. For computing QV, Illumina short reads were downloaded from https://www.ncbi.nlm.nih.gov/sra/?term=SRX1082031 for CHM13, https://ngdc.cncb.ac.cn/gsa/browse/CRA004538/CRX257577 for *A. thaliana*, and from https://www.ncbi.nlm.nih.gov/sra/SRX4381453[accn] for *M. musculus* (Sarsani et al. 2019).

The CHM13 reference (v1.1) can be downloaded from https://s3-us-west-2.amazonaws.com/human-pangenomics/T2T/CHM13/assemblies/chm13.draft_v1.1.fasta.gz. The *M. musculus* reference GRCm39 (strain C57BL/6J) is available at https://www.ncbi.nlm.nih.gov/datasets/genome/GCF_000001635.27/.

The *A. thaliana* reference Col-XJTU (strain Col-0) can be downloaded from https://download.cncb.ac.cn/gwh/Plants/Arabidopsis_thaliana_AT_GWHBDNP00000000.1/GWHBDNP00000000.1.genome.fasta.gz. The maternal *G. gallus* reference (isolate bGalGal1) is available at

https://www.ncbi.nlm.nih.gov/datasets/genome/GCF_016699485.2/. All the assemblies evaluated in this work are available at https://zenodo.org/records/13881591.

Software availability

Source code for GNNome framework (dataset construction, model training, and inference), together with the model weights, is available as Supplemental Code and at https://github.com/lbcb-sci/GNNome. The commands we used to run the tools discussed in this paper are available in Supplemental Note S6.

Acknowledgements

We thank Robert Vaser and Filip Tomas for help regarding Raven and Racon, especially for implementing functionality that helped our research. We also thank Haoyu Cheng who implemented graph-printing functionality into hifiasm. Finally, we thank Raden Indah Kendarsari for comments on the manuscript.

Lovro Vrček has been supported by "Young Researchers" Career Development Program DOK-2018-01-3373, ARAP scholarship awarded by A*STAR, and core funding of Genome Institute of Singapore, A*STAR. Xavier Bresson has been supported by NUS-R-252-000-B97-133. Martin Schmitz has been supported by SINGA scholarship awarded by A*STAR. Mile Šikić has been supported in part by the European Union through the European Regional Development Fund under the grant KK.01.1.1.01.0009 (DATACROSS), by the Croatian Science Foundation under the project Single genome and metagenome assembly (IP-2018-01-5886), and by the core funding of Genome Institute of Singapore, A*STAR.

562

563 Author contributions

564 M.Š. and X.B. led the research. L.V., X.B., T.L., and M.Š. developed the neural network architecture, training
565 pipeline, the decoding approach, and curated the data. L.V. implemented the framework, where X.B.
566 contributed to the training and decoding implementation, and M.S. implemented the algorithm for
567 determining the labels of edges in the training graphs. L.V., X.B., and M.Š. devised the experiments, while
568 L.V. performed them and analyzed the results. M.S. composed the figures. M.Š. and K.K. devised the
569 symmetric loss used during the training. M.Š. conceived the initial idea. L.V. and M.Š. wrote the paper,
570 while all the other authors provided feedback.

571

572 Competing interests

573 M.Š. has been jointly funded by Oxford Nanopore Technologies and AI Singapore for the project AI-driven
574 *De Novo* Diploid Assembler. The remaining authors declare no competing interests.

575

References

Brankovic L, Iliopoulos CS, Kundu R, Mohamed M, Pissis SP, Vayani F. 2016. Linear-time superbubble identification algorithm for genome assembly. *Theor Comput Sci* **609**: 374–383.

Bresson X, Laurent T. 2019. A two-step graph convolutional decoder for molecule generation. *arXiv [csLG]*. http://arxiv.org/abs/1906.03412.

Bresson X, Laurent T. 2017. Residual Gated Graph ConvNets. *arXiv [csLG]*. http://arxiv.org/abs/1711.07553.

Bronstein MM, Bruna J, Cohen T, Veličković P. 2021. Geometric Deep Learning: Grids, Groups, Graphs, Geodesics, and Gauges. *arXiv [csLG]*. http://arxiv.org/abs/2104.13478.

Cabanettes F, Klopp C. 2018. D-GENIES: dot plot large genomes in an interactive, efficient and simple way. *PeerJ* **6**: e4958.

Cheng H, Asri M, Lucas J, Koren S, Li H. 2024. Scalable telomere-to-telomere assembly for diploid and polyploid genomes with double graph. *Nat Methods*. http://dx.doi.org/10.1038/s41592-024-02269-8.

Cheng H, Concepcion GT, Feng X, Zhang H, Li H. 2021. Haplotype-resolved de novo assembly using phased assembly graphs with hifiasm. *Nat Methods* **18**: 170–175.

Cock PJA, Antao T, Chang JT, Chapman BA, Cox CJ, Dalke A, Friedberg I, Hamelryck T, Kauff F, Wilczynski B, et al. 2009. Biopython: freely available Python tools for computational molecular biology and bioinformatics. *Bioinformatics* **25**: 1422–1423.

Dwivedi VP, Joshi CK, Luu AT, Laurent T, Bengio Y, Bresson X. 2020. Benchmarking Graph Neural Networks. *arXiv [csLG]*. http://arxiv.org/abs/2003.00982.

596 Edmonds J, Johnson EL. 2003. Matching: A well-solved class of integer linear programs. In *Combinatorial*
597 *Optimization — Eureka, You Shrink!*, *Lecture notes in computer science*, pp. 27–30, Springer Berlin
598 Heidelberg, Berlin, Heidelberg.

599 Freeman TC, Horsewell S, Patir A, Harling-Lee J, Regan T, Shih BB, Prendergast J, Hume DA, Angus T. 2022.
600 Graphia: A platform for the graph-based visualisation and analysis of high dimensional data. *PLoS*
601 *Comput Biol* **18**: e1010310.

602 Garg S. 2021. Computational methods for chromosome-scale haplotype reconstruction. *Genome Biol* **22**:
603 101.

604 Garg S, Balboa R, Kuja J. 2022. Chromosome-scale haplotype-resolved pangenomics. *Trends Genet* **38**:
605 1103–1107.

606 Hagberg AA, Schult DA, Swart PJ. 2008. Exploring Network Structure, Dynamics, and Function using
607 NetworkX. In *Proceedings of the 7th Python in Science Conference* (eds. G. Varoquaux, T. Vaught,
608 and J. Millman), pp. 11–15, Pasadena, CA USA.

609 Hamilton WL, Ying R, Leskovec J. 2017. Inductive representation learning on large graphs. *arXiv [csSI]*.
610 http://arxiv.org/abs/1706.02216.

611 Harris CR, Millman KJ, van der Walt SJ, Gommers R, Virtanen P, Cournapeau D, Wieser E, Taylor J, Berg S,
612 Smith NJ, et al. 2020. Array programming with NumPy. *Nature* **585**: 357–362.

613 He X, Hooi B, Laurent T, Perold A, LeCun Y, Bresson X. 2022. A generalization of ViT/MLP-Mixer to graphs.
614 *arXiv [csCV]*. https://github.com/XiaoxinHe/Graph-ViT-MLPMixer.

615 Hon T, Mars K, Young G, Tsai Y-C, Karalius JW, Landolin JM, Maurer N, Kudrna D, Hardigan MA, Steiner CC,
616 et al. 2020. Highly accurate long-read HiFi sequencing data for five complex genomes. *Sci Data* **7**:
617 399.

618 Huang N, Li H. 2023. compleasm: a faster and more accurate reimplementation of BUSCO. *Bioinformatics*
619 **39**. http://dx.doi.org/10.1093/bioinformatics/btad595.

620 Idury RM, Waterman MS. 1995. A new algorithm for DNA sequence assembly. *J Comput Biol* **2**: 291–306.

621 Joshi CK, Laurent T, Bresson X. 2019. An efficient graph convolutional network technique for the Travelling
622 Salesman Problem. *arXiv [csLG]*. http://arxiv.org/abs/1906.01227.

623 Karypis G, Kumar V. 1998. A fast and high quality multilevel scheme for partitioning irregular graphs. *SIAM*
624 *J Sci Comput* **20**: 359–392.

625 Kingma DP, Ba J. 2014. Adam: A method for stochastic optimization. *arXiv [csLG]*.
626 http://arxiv.org/abs/1412.6980.

627 Kipf TN, Welling M. 2016. Semi-supervised classification with graph convolutional networks. *arXiv [csLG]*.
628 http://arxiv.org/abs/1609.02907.

629 Kolmogorov M, Yuan J, Lin Y, Pevzner PA. 2019. Assembly of long, error-prone reads using repeat graphs.
630 *Nat Biotechnol* **37**: 540–546.

631 Laurent T, von Brecht JH, Bresson X. 2022. Long-tailed learning requires feature learning. *arXiv [csLG]*.
632 http://arxiv.org/abs/2205.14553.

633 Li H. 2016. Minimap and miniasm: fast mapping and de novo assembly for noisy long sequences.
634 *Bioinformatics* **32**: 2103–2110.

635 Li H. 2018. Minimap2: pairwise alignment for nucleotide sequences. *Bioinformatics* **34**: 3094–3100.

636 Li H, Durbin R. 2024. Genome assembly in the telomere-to-telomere era. *Nat Rev Genet*.
637 http://dx.doi.org/10.1038/s41576-024-00718-w.

638 Li H, Feng X, Chu C. 2020. The design and construction of reference pangenome graphs with minigraph.
639 *Genome Biol* **21**: 265.

640 Makova KD, Pickett BD, Harris RS, Hartley GA, Cechova M, Pal K, Nurk S, Yoo D, Li Q, Hebbar P, et al. 2024.
641 The complete sequence and comparative analysis of ape sex chromosomes. *Nature* **630**: 401–411.

642 Mikheenko A, Prjibelski A, Saveliev V, Antipov D, Gurevich A. 2018. Versatile genome assembly evaluation
643 with QUAST-LG. *Bioinformatics* **34**: i142–i150.

644 Myers EW. 2005. The fragment assembly string graph. *Bioinformatics* **21 Suppl 2**: ii79-85.

645 Myers EW. 1995. Toward simplifying and accurately formulating fragment assembly. *J Comput Biol* **2**: 275–
646 290.

647 Navarro G. 2001. A guided tour to approximate string matching. *ACM Comput Surv* **33**: 31–88.

648 Nurk S, Koren S, Rhie A, Rautiainen M, Bzikadze AV, Mikheenko A, Vollger MR, Altemose N, Uralsky L,
649 Gershman A, et al. 2022. The complete sequence of a human genome. *Science* **376**: 44–53.

650 Nurk S, Walenz BP, Rhie A, Vollger MR, Logsdon GA, Grothe R, Miga KH, Eichler EE, Phillippy AM, Koren S.
651 2020. HiCanu: accurate assembly of segmental duplications, satellites, and allelic variants from
652 high-fidelity long reads. *Genome Res* **30**: 1291–1305.

653 Ono Y, Hamada M, Asai K. 2022. PBSIM3: a simulator for all types of PacBio and ONT long reads. *NAR*
654 *Genom Bioinform* **4**: lqac092.

Paszke A, Gross S, Massa F, Lerer A, Bradbury J, Chanan G, Killeen T, Lin Z, Gimelshein N, Antiga L, et al. 2019. PyTorch: An imperative style, high-performance deep learning library. In *Advances in Neural Information Processing Systems 32*, pp. 8024–8035, Curran Associates, Inc.

Peltola H, Söderlund H, Ukkonen E. 1984. SEQAID: a DNA sequence assembling program based on a mathematical model. *Nucleic Acids Res* **12**: 307–321.

Pevzner PA, Tang H, Waterman MS. 2001. An Eulerian path approach to DNA fragment assembly. *Proc Natl Acad Sci U S A* **98**: 9748–9753.

Rautiainen M, Nurk S, Walenz BP, Logsdon GA, Porubsky D, Rhie A, Eichler EE, Phillippy AM, Koren S. 2023. Telomere-to-telomere assembly of diploid chromosomes with Verkko. *Nat Biotechnol* **41**: 1474–1482.

Rossi E, Charpentier B, Di Giovanni F, Frasca F, Günnemann S, Bronstein M. 2023. Edge directionality improves learning on heterophilic graphs. *arXiv [csLG]*. http://arxiv.org/abs/2305.10498.

Sarsani VK, Raghupathy N, Fiddes IT, Armstrong J, Thibaud-Nissen F, Zinder O, Bolisetty M, Howe K, Hinerfeld D, Ruan X, et al. 2019. The genome of C57BL/6J “Eve”, the mother of the laboratory mouse genome reference strain. *G3 (Bethesda)* **9**: 1795–1805.

Scarselli F, Gori M, Tsoi AC, Hagenbuchner M, Monfardini G. 2009. The graph neural network model. *IEEE Trans Neural Netw* **20**: 61–80.

Shafin K, Pesout T, Lorig-Roach R, Haukness M, Olsen HE, Bosworth C, Armstrong J, Tigyi K, Maurer N, Koren S, et al. 2020. Nanopore sequencing and the Shasta toolkit enable efficient de novo assembly of eleven human genomes. *Nat Biotechnol* **38**: 1044–1053.

675 Shen W, Le S, Li Y, Hu F. 2016. SeqKit: A cross-platform and ultrafast toolkit for FASTA/Q file manipulation.
676 *PLoS One* **11**: e0163962.

677 Šošić M, Šikić M. 2017. Edlib: a C/C++ library for fast, exact sequence alignment using edit distance.
678 *Bioinformatics* **33**: 1394–1395.

679 Van Rossum G, Drake FL Jr. 2009. *Python 3 Reference Manual*. Createspace.

680 Vaser R, Šikić M. 2021. Time- and memory-efficient genome assembly with Raven. *Nature Computational*
681 *Science* **1**: 332–336.

682 Vaser R, Sović I, Nagarajan N, Šikić M. 2017. Fast and accurate de novo genome assembly from long
683 uncorrected reads. *Genome Res* **27**: 737–746.

684 Veličković P, Cucurull G, Casanova A, Romero A, Liò P, Bengio Y. 2017. Graph Attention Networks. *arXiv*
685 *[statML]*. http://arxiv.org/abs/1710.10903.

686 Vrček L, Bresson X, Laurent T, Schmitz M, Šikić M. 2022. Learning to untangle genome assembly with graph
687 convolutional networks. *arXiv [q-bioGN]*. http://arxiv.org/abs/2206.00668.

688 Wang B, Yang X, Jia Y, Xu Y, Jia P, Dang N, Wang S, Xu T, Zhao X, Gao S, et al. 2022a. High-quality Arabidopsis
689 thaliana Genome Assembly with Nanopore and HiFi Long Reads. *Genomics Proteomics*
690 *Bioinformatics* **20**: 4–13.

691 Wang M, Zheng D, Ye Z, Gan Q, Li M, Song X, Zhou J, Ma C, Yu L, Gai Y, et al. 2019. Deep Graph Library: A
692 graph-centric, highly-performant package for graph neural networks. *arXiv [csLG]*.
693 http://arxiv.org/abs/1909.01315.

694 Wang T, Antonacci-Fulton L, Howe K, Lawson HA, Lucas JK, Phillippy AM, Popejoy AB, Asri M, Carson C,
695 Chaisson MJP, et al. 2022b. The Human Pangenome Project: a global resource to map genomic
696 diversity. *Nature* **604**: 437–446.

697 Zerbino DR, Birney E. 2008. Velvet: algorithms for de novo short read assembly using de Bruijn graphs.
698 *Genome Res* **18**: 821–829.

699